

# On-Load Field Prediction of Surface-Mounted PM Machines Considering Nonlinearity Based on Hybrid Field Model

L. J. Wu<sup>1</sup>, Zhaokai Li<sup>1</sup>, Dong Wang<sup>2</sup>, Hao Yin<sup>1</sup>, Xiaoyan Huang<sup>1</sup>, and Z. Q. Zhu<sup>3</sup>

<sup>1</sup>College of Electrical Engineering, Zhejiang University, Hangzhou 310027, China

<sup>2</sup>National Key Laboratory of Science and Technology on Vessel Integrated Power System, Naval University of Engineering, Wuhan 430000, China

<sup>3</sup>Department of Electronic and Electrical Engineering, The University of Sheffield, S13JD Sheffield, U.K.

Analytical models show weakness in dealing with saturation in surface-mounted permanent-magnet machines. A hybrid field model (HFM) integrating complex permeance method (CPM) and lumped parameter magnetic circuit model (LPMCM) is proposed in this paper for predicting the on-load magnetic field considering nonlinearity effect of stator lamination. In the proposed model, the CPM calculates the field in the air gap and magnet regions, while LPMCM calculates the magnetic potential distribution inside the iron reflecting nonlinearity effect. The equivalent current sheet is obtained to replace such distribution on the stator bore. Moreover, local magnetic saturation of tooth tip is also transformed into equivalent current on the tooth surface. A solving procedure is proposed to calculate the equivalent current and guarantee the convergence. Compared with CPM, the proposed model considering the saturation effect significantly improves the prediction accuracy of the on-load performance. The HFM predictions are compared with finite element and experimental results. The excellent agreement validates its effectiveness.

**Index Terms**—Analytical model, complex permeance, magnetic equivalent circuit, saturation effect, surface-mounted permanent-magnet (SPM) machines.

## I. INTRODUCTION

PERMANENT-MAGNET (PM) machines become increasingly popular benefiting from their high torque density and efficiency [1]. Therefore, researchers have made a great effort in developing accurate and fast tools for analysis, design, and optimization of such machines. Although numerical methods are accurate, it is very time-consuming and provides little straightforward physical insight into machine design [2]. On the contrary, many analytical models are available to quickly reveal the physical relationship between the geometry of PM machines and their performance [3]–[9]. They are accurate for machines with linear materials. However, machine designers usually push work point of an iron material to or slightly over the knee point of its  $B$ – $H$  curve in order to achieve better torque density. Hence, the analytical models lack high accuracy for these machines because of neglecting nonlinearity effect.

The preference of both the high computational speed and accuracy motivates the integration of analytical models with numerical methods. There are many potential candidates for such integration. For analytical models, a complex permeance model is a good option. Zhu *et al.* [3], [4] analytically calculated the field in the air gap/magnet regions for slotless PM machines. The stator slotting effect can be taken into account by conformal mapping. Typical examples can be found in [5], which gives the calculation of complex permeance function to consider slotting effect on both the radial

and circumferential components of flux density. It is simple and fast because Schwarz–Christoffel (SC) transformation is required only once, but it neglects the deformation of magnets and path for air gap field prediction. To eliminate this error, exact conformal mapping based on SC Toolbox can be used to accurately calculate the magnetic field in the surface-mounted PM (SPM) machines [7], [8]. SC Toolbox was developed to construct an SC map from the machine geometry at first and then numerically evaluate the position of PM equivalent current in the canonical domain at every rotor position [10]. Hence, it is very time-consuming. On the other hand, the lumped parameter magnetic circuit model (LPMCM) is a good option for numerical method since both the finite element (FE) and finite difference methods require large calculation and are not preferred. The LPMCM is fast and very effective for the path in the iron, but often shows difficulty for the path in the air. It is because the flux tube in the air has a complicated shape, which can be varying with the rotor position [11], [12]. It is particularly difficult for the air gap and magnet regions in SPM machines, in which the surface of the magnet does not show equal potential. The area of LPMCMs weakness is exactly the strong side of analytical models. Therefore, the integration of complex permeance method (CPM) and LPMCM can provide both the high computational speed and accuracy.

In order to account for iron nonlinearity, some analytical models are modified to account for the magnetic potential distribution in the iron. Dalal and Kumar [13] obtained the air-gap field distribution by solving Laplace/quasi-Poissonian equations in six regions, of which the stator core permeability is assumed a linear function of the load angle. However, such linear function is found by using FE method (FEM), and the whole stator iron is assumed the constant permeability. On the other hand, LPMCM is often used to analyze the nonlinear

Manuscript received July 15, 2018; revised October 14, 2018 and December 4, 2018; accepted December 6, 2018. Date of publication January 31, 2019; date of current version February 15, 2019. Corresponding author: Z. Q. Zhu (e-mail: z.q.zhu@sheffield.ac.uk).

Color versions of one or more of the figures in this paper are available online at <http://ieeexplore.ieee.org>.

Digital Object Identifier 10.1109/TMAG.2018.2890244

0018-9464 © 2019 IEEE. Personal use is permitted, but republication/redistribution requires IEEE permission.

See [http://www.ieee.org/publications\\_standards/publications/rights/index.html](http://www.ieee.org/publications_standards/publications/rights/index.html) for more information.

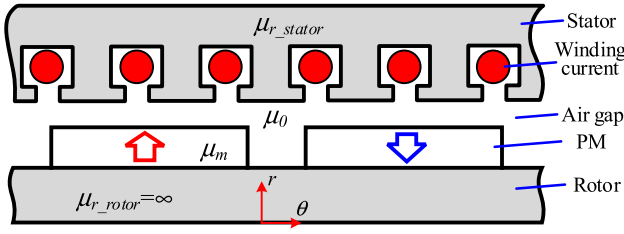


Fig. 1. Schematic of SPM machine.

iron core. From the LPMCM solution, the air-gap length and slot opening are modified to represent the magnetic potential drops of the stator [14]–[16]. Then, the complex permeance based on the modified air gap and slot opening was introduced to account for both the saturation effect and slotting effect. Nevertheless, these models in [14]–[16] are time-consuming due to the calculation of the saturated complex permeance using SC transformation at every rotor position.

In addition, equivalent virtual current is powerful in magnetic field calculation. It has been widely used to replace the PM and calculate the electromagnetic performance in many PM machines such as interior permanent magnet (IPM) machine [17], transverse flux machine [18], and eccentric SPM machine [19]. For the saturated SPM machine, Hanic *et al.* [20], [21] combined the conformal mapping and LPMCM to analyze the air-gap field by using equivalent currents. The SC mapping in [20] and [21] transforms the slotted domain with equivalent current sheets of magnets into the slotless domain. The field distribution due to winding current and magnet equivalent currents placed at the new mapped positions is calculated by using Hague's solution. It is then transformed back into the original slotted domain. In [22], the CPM instead of exact conformal mapping in [20] and [21] is combined with LPMCM to predict the open-circuit field of SPM machines, but the analysis of on-load field is not included as well as the consideration of tooth-tip saturation, which is common and important in electric machines. Hence, this paper will investigate the on-load field of SPM machines accounting for slot flux leakage. Most importantly, the tooth-tip saturation will be analyzed in this paper.

A hybrid field model (HFM) integrating CPM and LPMCM is presented for the on-load field prediction in SPM machines with tooth tips. Such combination is based on the equivalence between the magnetic potential drop in the stator and virtual current along the stator bore. In order to calculate the virtual current representing nonlinearity effect, a solving procedure based on the Newton–Raphson method is developed to guarantee the convergence in the iteration. Both the FE analysis and experiment are implemented to verify the proposed model.

## II. HYBRID FIELD MODEL

Assumptions are made to ease modeling: 1) PM has a linear recoil line; 2) the end effect is neglected; and 3) the rotor iron is infinitely permeable. As for some cases that rotor iron saturation cannot be neglected, the model should be reconstructed.

Fig. 1 shows the schematic of an SPM machine; whose stator iron has a nonlinear permeability. When a different

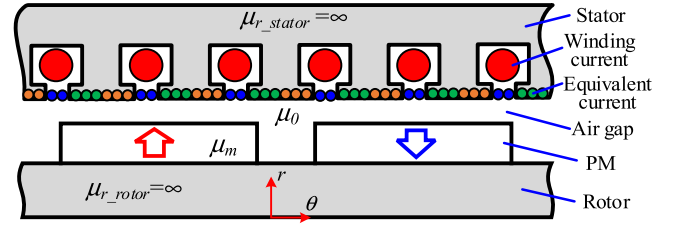


Fig. 2. HFM of slotted SPM machine considering nonlinearity effect under on-load condition.

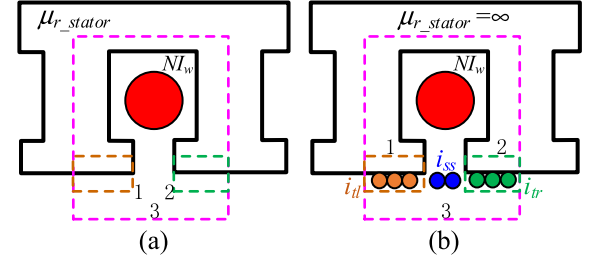


Fig. 3. Ampere loops in (a) initial nonlinear model and (b) equivalent model with equivalent current.

level of excitation from PM and winding current is applied, there will be different work point of stator iron on the  $B$ – $H$  curve, namely, different relative permeability  $\mu_{r\_stator}$ . Since the analytical model is not applicable to the nonlinear model in Fig. 1, it has to be equivalently transformed into an infinitely permeable model, whose magnetic potential drop in the stator becomes zero. In order to compensate the magnetic potential drop in the stator of an infinitely permeable model, virtual equivalent current is introduced to represent the nonlinearity effect, as shown in Fig. 2. It is noted that the virtual current at the slot opening is used to consider the saturation of stator yoke and teeth body while the virtual current at the teeth surface is presented to show the tooth-tip saturation. Fig. 3 shows the justification for introducing the virtual current. Along the loop 1 in Fig. 3(a), Ampere's law can be applied as

$$F_{tip1} + \int_{L_{airgap1}} H_{airgap1} dl = 0 \quad (1)$$

where  $F_{tip1}$  is the magnetic potential drop across the tooth tip 1,  $L_{airgap1}$  is the air-gap path of loop 1, and  $H_{airgap1}$  is the magnetic field along  $L_{airgap1}$ .

In Fig. 3(b), Ampere's law can give

$$0 + \int_{L_{airgap1}} H_{airgap1} dl = i_{tl}. \quad (2)$$

In order to keep  $H_{airgap1}$  unchanged, the equivalent current should satisfy

$$i_{tl} = -F_{tip1}. \quad (3)$$

Similarly

$$i_{tr} = -F_{tip2} \quad (4)$$

where  $i_{tl}$  and  $i_{tr}$  are the equivalent currents at the left and right sides of tooth shoe.

Along the loop 3 in Fig. 3(a), according to Ampere's law

$$F_{tooth1} + F_{yoke} + F_{tooth2} + \int_{L_{airgap3}} H_{airgap3} dl = NI_w \quad (5)$$

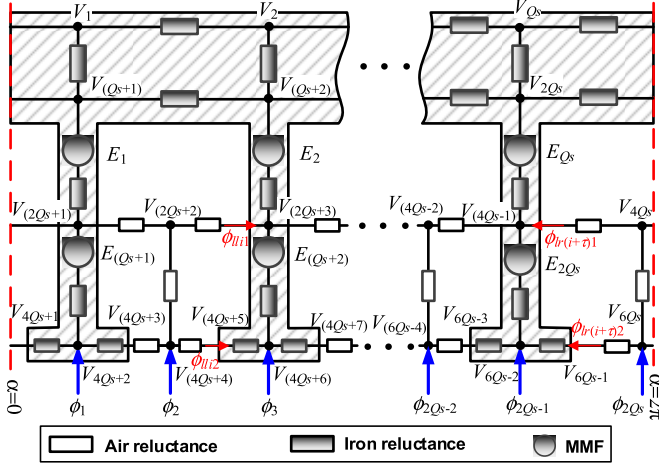


Fig. 4. Equivalent magnetic network of the stator.

where  $F_{\text{tooth1}}$ ,  $F_{\text{tooth2}}$ , and  $F_{\text{yoke}}$  are, respectively, the magnetic potential drops across the tooth 1, tooth 2, and yoke;  $I_w$  is the winding current; and  $N$  is the number of turns.

For the same loop in Fig. 3(b), Ampere's law can give

$$0 + \int_{L_{\text{airgap3}}} H_{\text{airgap3}} dl = NI_w + i_{tl} + i_{tr} + i_{ss}. \quad (6)$$

In order to keep  $H_{\text{airgap3}}$  unchanged, the equivalent current at the slot opening should be

$$i_{ss} = -(F_{\text{tooth1}} + F_{\text{yoke}} + F_{\text{tooth2}}) - (i_{tl} + i_{tr}). \quad (7)$$

Hence, the infinitely permeable model can be analytically solved considering iron nonlinearity by equivalent currents.

#### A. Equivalent Current Representing Stator Nonlinearity

The equivalent current, which represents the nonlinearity effect, is the keypoint in the HFM. It is calculated from the magnetic potential distribution of LPMCM. Fig. 4 shows that the magnetic reluctances representing the nonlinear property of the stator iron are connected to establish a magnetic network.  $V_1, V_2, \dots, V_{6Qs}$  are the node magnetic potential in the LPMCM, where  $Q_s$  is the slot number. The air-gap flux  $\phi_j$  flowing into the stator is expressed as

$$\phi_j = \int_{s_j} B_{sr}(R_s) ds \quad (8)$$

where  $s_j$  is the area of the slot or tooth on the stator bore,  $j$  is the index of the slot and tooth ( $j = 1, 2, \dots, 2Q_s$ ),  $R_s$  is the stator bore radius, and  $B_{sr}(R_s)$  is the radial flux density on the stator bore.

According to KCL, the node magnetic potential is obtained by

$$f(\mathbf{V}) = \mathbf{A}\mathbf{\Lambda}(\mathbf{A}^T\mathbf{V} - \mathbf{E}) - \mathbf{A}\Phi = 0 \quad (9)$$

where  $\Phi$  is the branch flux matrix which includes  $\phi_j$  for the fluxes into stator and 0 for the rest branches.  $\mathbf{A}$ ,  $\mathbf{\Lambda}$ , and  $\mathbf{V}$  are the matrixes of the incidence, branch permeance, and

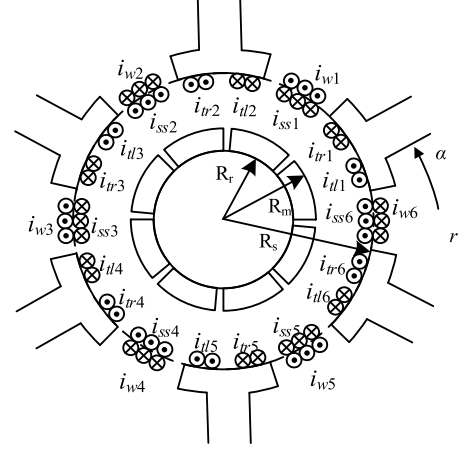


Fig. 5. Illustration of equivalent current sheet.

node magnetic potential, respectively. The permeance in  $\mathbf{\Lambda}$  is calculated using the following equation [11] and [12]:

$$\begin{aligned} p_r &= \frac{\mu l_{ef} a}{b} \\ p_{sr} &= \frac{\mu l_{ef} \alpha_0}{\ln(R_2/R_1)} \\ p_{st} &= \frac{\mu l_{ef} \ln(R_2/R_1)}{\alpha_0} \end{aligned} \quad (10)$$

where  $p_r$ ,  $p_{sr}$ , and  $p_{st}$  are the permeance of the rectangular material, radial sector material, and tangential sector material, respectively.  $\mu$  is the permeability of the material and  $l_{ef}$  is the active length.  $a$  is the width of the cross-sectional area and  $b$  is the length along the flux direction in the rectangle.  $\alpha_0$ ,  $R_1$ , and  $R_2$  are the central angle, outer radius, and inner radius of the sector. It can be seen that  $p_r$  is suitable to calculate the tooth permeance in the LPMCM while  $p_{sr}$  and  $p_{st}$  is intended for the radial and tangential permeance of stator yoke, tooth shoe, slot, and slot opening.  $\mathbf{E}$  is the branch MMF matrix calculated by winding current [11]

$$\begin{cases} E_{2Q_s} = E_{Q_s} = -\frac{1}{2Q_s} \sum_{n=1}^{Q_s-1} (Q_s - n) i_{wn} \\ E_{Q_s+1} = E_1 = E_{Q_s} + \frac{i_{w1}}{2} \\ E_{Q_s+2} = E_2 = E_1 + \frac{i_{w2}}{2} \\ \dots \\ E_{2Q_s-1} = E_{Q_s-1} = E_{Q_s-2} + \frac{i_{w(Q_s-1)}}{2} \end{cases} \quad (11)$$

where  $E_1, E_2, \dots, E_{2Q_s}$  are the values of branch MMF which forms  $\mathbf{E}$  and  $i_{w1}, i_{w2}, \dots, i_{w(Q_s-1)}$  are the winding current.

The equivalent currents are illustrated in Fig. 5. The equivalent current on the  $k$ th slot opening is obtained by

$$i_{ssk} + i_{wk} = -(V_{m+2} - V_m) \quad (12)$$

where  $i_{ssk}$  and  $i_{wk}$  are the equivalent and winding currents in the  $k$ th slot, respectively,  $k$  is the index of tooth and slot,  $k = 1, 2, \dots, Q_s$ ,  $V_m$ , and  $V_{m+2}$  are the magnetic potentials of nodes at the left and right sides of the  $k$ th slot opening. It is noted that  $V_{m+2}$  and  $V_m$  in the right-hand side of (12) are calculated from the nonlinear model, while  $i_{ssk}$  and  $i_{wk}$  in the

left-hand side of (12) are intended for the infinitely permeable model.

Considering the nonlinearity effect in the tooth tip, the virtual current on the tooth shoe should be added in the infinitely permeable model. In addition, the virtual current value on the tooth shoe should be equal to the magnetic potential drop along the tooth shoe in order to produce the same air gap field

$$\begin{cases} i_{tlk} = -(V_{m-1} - V_{m-2}) \\ i_{trk} = -(V_m - V_{m-1}) \end{cases} \quad (13)$$

where  $i_{tlk}$  and  $i_{trk}$  are the equivalent currents at the left and right sides of the  $k$ th tooth shoe,  $V_{m-1}$  is the magnetic potential on the node in the middle of the  $k$ th tooth top,  $V_{m-2}$  and  $V_m$  are the magnetic potential on the nodes at the left and right sides of the  $k$ th tooth tip, respectively. Then, (12) and (13) can be expressed in the matrix form

$$\begin{cases} \mathbf{I}_{ss} + \mathbf{I}_w = \mathbf{C}_{ss}\mathbf{V} \\ \mathbf{I}_{tl} = \mathbf{C}_{tl}\mathbf{V} \\ \mathbf{I}_{tr} = \mathbf{C}_{tr}\mathbf{V} \end{cases} \quad (14)$$

where  $\mathbf{C}_{ss}$ ,  $\mathbf{C}_{tl}$ , and  $\mathbf{C}_{tr}$  are the constant matrixes calculated from (12) and (13) and

$$\mathbf{I}_{ss} = [i_{ss1} \ i_{ss2} \ \cdots \ i_{ssQ_s}]^T \quad (15)$$

$$\mathbf{I}_w = [i_{w1} \ i_{w2} \ \cdots \ i_{wQ_s}]^T \quad (16)$$

$$\mathbf{I}_{tl} = [i_{tl1} \ i_{tl2} \ \cdots \ i_{tlQ_s}]^T \quad (17)$$

$$\mathbf{I}_{tr} = [i_{tr1} \ i_{tr2} \ \cdots \ i_{trQ_s}]^T. \quad (18)$$

### B. Slotted Air-Gap Field Solution

Since the equivalent current is introduced to represent the nonlinearity effect, the stator iron becomes infinitely permeable, as shown in Fig. 2. Thus, the analytical model with the assumption of infinitely permeable iron is suitable to calculate the magnetic field of SPM machines. As for the slotting effect, CPM based on conformal mapping is used to calculate the slotted air gap field from the slotless air-gap field [5]

$$\begin{aligned} B_{sr} &= B_r \lambda_r + B_\alpha \lambda_i \\ B_{sa} &= B_\alpha \lambda_r - B_r \lambda_i \end{aligned} \quad (19)$$

where  $B_{sr}$  and  $B_{sa}$  are the radial and circumferential slotted air-gap flux density, respectively.  $\lambda_r$  and  $\lambda_i$  are the real and imaginary components of complex permeance, whose calculation is described in [22].  $B_r$  and  $B_\alpha$  are the radial and circumferential slotless air-gap flux density, which are obtained by superposition of the field components produced by the PM, winding, and equivalent currents with infinitely permeable iron (Fig. 6)

$$\begin{aligned} B_r(\alpha, r, t) &= B_{mr}(\theta, r) + B_{wr}(\alpha, r, t) + B_{sat_r}(\alpha, r, t) \\ &= B_{mr}(\theta, r) + B_{cr}(\alpha, r, t) \end{aligned} \quad (20)$$

$$\begin{aligned} B_\alpha(\alpha, r, t) &= B_{ma}(\theta, r) + B_{wa}(\alpha, r, t) + B_{sat_\alpha}(\alpha, r, t) \\ &= B_{ma}(\theta, r) + B_{ca}(\alpha, r, t) \end{aligned} \quad (21)$$

where  $B_{mr}$  and  $B_{ma}$  are the radial and circumferential flux density components due to the PM;  $B_{wr}$  and  $B_{wa}$  are the

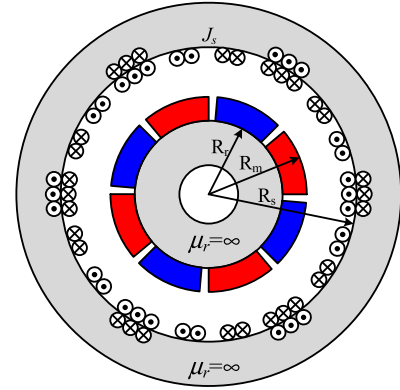


Fig. 6. HFM of slotless SPM machine.

radial and circumferential flux density components due to the winding current;  $B_{sat_r}$  and  $B_{sat_\alpha}$  are the radial and circumferential flux density components due to the equivalent current.  $\alpha$  and  $\theta$  are the stator and rotor angular positions, respectively, and  $\theta = \omega_r t + \theta_0$ , where  $\theta_0$  is the initial position of the rotor and  $\omega_r$  is the mechanical angular velocity.

The solution of the slotless air-gap field due to PMs neglecting nonlinearity effect was derived in [22]. Therefore, this paper only gives the final expressions of radial and circumferential air-gap flux density components

$$B_{mr}(\theta, r) = \sum_{n=1,3,5,\dots}^{\infty} K_B(n) f_{Br}(r) \cos(np\theta) \quad (22)$$

$$B_{ma}(\theta, r) = \sum_{n=1,3,5,\dots}^{\infty} K_B(n) f_{B\theta}(r) \sin(np\theta) \quad (23)$$

where  $K_B(n)$ ,  $f_{Br}(r)$ , and  $f_{B\theta}(r)$  are given in [22].

As for the magnetic field produced by stator current including winding current and equivalent current of saturation neglecting saturation effect, the governing Laplacian equation in the air-gap region is

$$\frac{\partial^2 \varphi}{\partial r^2} + \frac{1}{r} \frac{\partial \varphi}{\partial r} + \frac{1}{r^2} \frac{\partial^2 \varphi}{\partial \alpha^2} = 0 \quad (24)$$

and the boundary condition is [4]

$$\begin{cases} B_\alpha|_{r=R_r} = 0 \\ H_\alpha|_{r=R_s} = -J_s \end{cases} \quad (25)$$

where  $R_r$  is the rotor yoke surface radius and  $J_s$  is the resultant of winding and equivalent currents, which can be expressed as Fourier series from Fig. 5

$$\begin{aligned} J_s &= \sum_{k=1}^{Q_s} \sum_v \frac{2(i_{ssk} + i_{wk})}{\pi b_0} \frac{1}{v} \sin\left(\frac{vb_0}{2R_s}\right) \cos\left[v\left(\alpha - \frac{2k\pi}{Q_s}\right)\right] \\ &+ \sum_{k=1}^{Q_s} \sum_v \frac{4i_{tlk}}{\pi t_0} \frac{1}{v} \sin\left(\frac{vt_0}{4R_s}\right) \\ &\times \cos\left[v\left(\alpha - \frac{(2k-1)\pi}{Q_s} + \frac{t_0}{4R_s}\right)\right] \\ &+ \sum_{k=1}^{Q_s} \sum_v \frac{4i_{trk}}{\pi t_0} \frac{1}{v} \sin\left(\frac{vt_0}{4R_s}\right) \\ &\times \cos\left[v\left(\alpha - \frac{(2k-1)\pi}{Q_s} - \frac{t_0}{4R_s}\right)\right] \end{aligned} \quad (26)$$



where  $b_0$  is the slot-opening width and  $t_0$  is the tooth top width.

By solving the governing Laplacian equation with the boundary condition, the radial and circumferential flux density components due to the stator current can be given by

$$B_{cr} = \frac{\mu_0}{\pi} \sum_{k=1}^{Q_s} \sum_v \left\{ \frac{i_{ssk} + i_{wk}}{v} K_{sov}(b_0) F_v(r) \right. \\ \times \sin \left[ v \left( \alpha - \frac{2k\pi}{Q_s} \right) \right] \\ + \frac{i_{tlk}}{v} K_{sov} \left( \frac{t_0}{2} \right) F_v(r) \\ \times \sin \left[ v \left( \alpha - \frac{(2k-1)\pi}{Q_s} + \frac{t_0}{4R_s} \right) \right] \\ + \frac{i_{trk}}{v} K_{sov} \left( \frac{t_0}{2} \right) F_v(r) \\ \times \sin \left[ v \left( \alpha - \frac{(2k-1)\pi}{Q_s} - \frac{t_0}{4R_s} \right) \right] \left. \right\} \quad (27)$$

$$B_{ca} = \frac{\mu_0}{\pi} \sum_{k=1}^{Q_s} \sum_v \left\{ \frac{i_{ssk} + i_{wk}}{v} K_{sov}(b_0) G_v(r) \right. \\ \times \cos \left[ v \left( \alpha - \frac{2k\pi}{Q_s} \right) \right] \\ + \frac{i_{tlk}}{v} K_{sov} \left( \frac{t_0}{2} \right) G_v(r) \\ \times \cos \left[ v \left( \alpha - \frac{(2k-1)\pi}{Q_s} + \frac{t_0}{4R_s} \right) \right] \\ + \frac{i_{trk}}{v} K_{sov} \left( \frac{t_0}{2} \right) G_v(r) \\ \times \cos \left[ v \left( \alpha - \frac{(2k-1)\pi}{Q_s} + \frac{t_0}{4R_s} \right) \right] \left. \right\} \quad (28)$$

where  $F_v$ ,  $G_v$ , and  $K_{sov}$  are

$$F_v(r) = \frac{v}{r} \left( \frac{r}{R_s} \right)^v \frac{1 + (R_r/r)^{2v}}{1 - (R_r/R_s)^{2v}} \quad (29)$$

$$G_v(r) = \frac{v}{r} \left( \frac{r}{R_s} \right)^v \frac{1 - (R_r/r)^{2v}}{1 - (R_r/R_s)^{2v}} \quad (30)$$

$$K_{sov}(\beta) = \frac{\sin(v\beta/2R_s)}{v\beta/2R_s}. \quad (31)$$

### C. Convergent Solving Procedure

In the proposed HFM, the air-gap field solution and calculation of equivalent current depend on each other. Therefore, a solving procedure is proposed to iteratively calculate the equivalent current as well as air gap field and guarantee the convergence in one loop. The basic idea is to incorporate the air-gap analytical solution into the procedure of solving the LPMCM. Therefore, in the LPMCM, the air-gap flux  $\varphi_j$

flowing into the stator is rederived from (8)

$$\varphi_j = \sum_{k=1}^{Q_s} [g_{ssk}(s_j)(i_{ssk} + i_{wk}) + g_{tlk}(s_j)i_{tlk} \\ + g_{trk}(s_j)i_{trk}] + \int_{s_j} (\lambda_r B_{mr} + \lambda_i B_{ma}) ds \\ = \mathbf{G}_{ss}(s_j)(\mathbf{I}_{ss} + \mathbf{I}_w) + \mathbf{G}_{tl}(s_j)\mathbf{I}_{tl} + \mathbf{G}_{tr}(s_j)\mathbf{I}_{tr} + \varphi_m(s_j) \quad (32)$$

where  $g_{ssk}$ ,  $g_{tlk}$ , and  $g_{trk}$  are calculated from (19)–(31) and

$$\mathbf{G}_{ss}(s_j) = [g_{ss1}(s_j) \quad g_{ss2}(s_j) \quad \cdots \quad g_{ssQ_s}(s_j)] \quad (33)$$

$$\mathbf{G}_{tl}(s_j) = [g_{tl1}(s_j) \quad g_{tl2}(s_j) \quad \cdots \quad g_{tlQ_s}(s_j)] \quad (34)$$

$$\mathbf{G}_{tr}(s_j) = [g_{tr1}(s_j) \quad g_{tr2}(s_j) \quad \cdots \quad g_{trQ_s}(s_j)] \quad (35)$$

$$\varphi_m(s_j) = \int_{s_j} (\lambda_r B_{mr} + \lambda_i B_{ma}) ds. \quad (36)$$

The equivalent current  $\mathbf{I}_{ss} + \mathbf{I}_w$ ,  $\mathbf{I}_{tl}$ , and  $\mathbf{I}_{tr}$  in (32) can be calculated from the magnetic potential distribution of LPMCM according to (14). Thus,  $\varphi_j$  in (32) is a function of the magnetic potential distribution  $\mathbf{V}$

$$\varphi_j = (\mathbf{G}_{ss}(s_j)\mathbf{C}_{ss} + \mathbf{G}_{tl}(s_j)\mathbf{C}_{tl} + \mathbf{G}_{tr}(s_j)\mathbf{C}_{tr}) \mathbf{V} + \varphi_m(s_j). \quad (37)$$

It can also be expressed in the matrix form as

$$\Phi = (\mathbf{R}_{ss}\mathbf{C}_{ss} + \mathbf{R}_{tl}\mathbf{C}_{tl} + \mathbf{R}_{tr}\mathbf{C}_{tr}) \mathbf{V} + \Phi_m \quad (38)$$

where

$$\mathbf{R}_{ss} = [\mathbf{G}_{ss}(s_1) \quad \mathbf{G}_{ss}(s_2) \quad \cdots \quad \mathbf{G}_{ss}(s_{2Q_s})]^T \quad (39)$$

$$\mathbf{R}_{tl} = [\mathbf{G}_{tl}(s_1) \quad \mathbf{G}_{tl}(s_2) \quad \cdots \quad \mathbf{G}_{tl}(s_{2Q_s})]^T \quad (40)$$

$$\mathbf{R}_{tr} = [\mathbf{G}_{tr}(s_1) \quad \mathbf{G}_{tr}(s_2) \quad \cdots \quad \mathbf{G}_{tr}(s_{2Q_s})]^T \quad (41)$$

$$\Phi_m = [\varphi_m(s_1) \quad \varphi_m(s_2) \quad \cdots \quad \varphi_m(s_{2Q_s})]^T. \quad (42)$$

Thus, according to (9), the general solution for LPMCM can be obtained by

$$f(\mathbf{V}) = \mathbf{A}[\mathbf{\Lambda}\mathbf{A}^T - (\mathbf{R}_{ss}\mathbf{C}_{ss} + \mathbf{R}_{tl}\mathbf{C}_{tl} + \mathbf{R}_{tr}\mathbf{C}_{tr})]\mathbf{V} \\ - \mathbf{A}\mathbf{\Lambda}\mathbf{E} - \mathbf{A}\Phi_m = \mathbf{0}. \quad (43)$$

It can be seen from (43) that only branch permeance matrix  $\mathbf{\Lambda}$  depends on the magnetic potential distribution. Hence, only one loop is required to solve the “new” LPMCM using  $B$ – $H$  curves. Fig. 7 shows the general flowchart to calculate the equivalent current and air gap flux densities. In fact, the essence of HFM is to replace the inaccurate modeling of air gap reluctance in LPMCM with virtual reluctance ( $\mathbf{R}_{ss}$ ,  $\mathbf{R}_{tl}$ , and  $\mathbf{R}_{tr}$ ) and flux source ( $\Phi_m$ ) from the air-gap field solution of CPM. Meanwhile, the air-gap magnetic network of HFM is also a Norton equivalent circuit compared to the original LPMCM, which proves the validity of the proposed replacement.

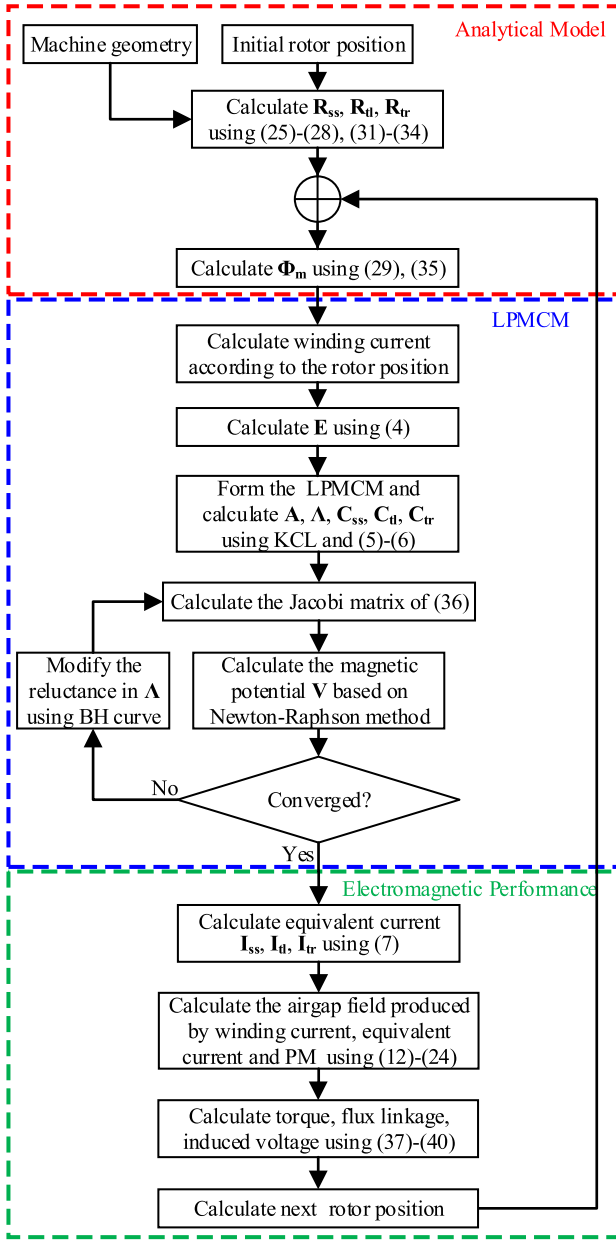


Fig. 7. General flowchart of calculation procedure.

#### D. Speed and Accuracy in Calculation

The tradeoff between speed and accuracy in the calculation of electromagnetic field is an unavoidable issue for researchers to analyze. Thus, it is necessary to compare and investigate the speed and accuracy of CPM, FEM, and HFM in the air-gap field prediction. CPM neglects the core saturation and requires no iteration process at any rotor position. Therefore, it is the fastest but also least accurate compared with other methods. On the contrary, FEM shows the highest accuracy in predicting the magnetic field and, therefore, is often employed to verify the accuracy of the analytical model for the electrical machines [17]–[21]. However, it is also the most time-consuming method because it needs to iteratively solve an  $N_{\text{fem}} \times N_{\text{fem}}$  nonlinear matrix, where  $N_{\text{fem}}$  represents the number of FE nodes and is always very large for accurate

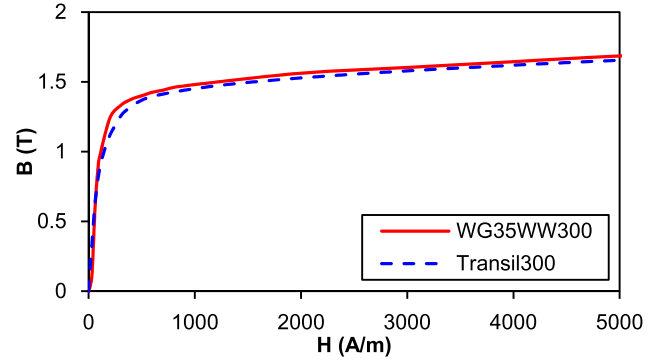


Fig. 8. B–H curves of the iron of both machines.

calculation. As for HFM, it combines the advantage of both the CPM and LPMCM with high speed and great accuracy. Due to considering nonlinear property of iron core, the accuracy of magnetic field prediction is greatly improved compared with CPM, especially when the machine is highly saturated. In addition, the calculation time of HFM is theoretically shorter than FEM because HFM only solves a much smaller  $N_{\text{mcm}} \times N_{\text{mcm}}$  matrix, where  $N_{\text{mcm}}$  represents the number of nodes in the LPMCM.

### III. ELECTROMAGNETIC PERFORMANCE

The main flux of a coil can be calculated from the air-gap field distribution

$$\varphi_i(t) = R_s l_{ef} \int_{\alpha_i - \tau/2 + b_0/R_s}^{\alpha_i + \tau/2 - b_0/R_s} B_{sr}(\alpha, R_s, t) d\alpha \quad (44)$$

where  $\alpha_i$  and  $\tau$  are, respectively, the circumferential position and coil pitch of such coil.

By summing the flux linkages associated with all coils from the same phase, the flux linkage  $\psi_{\text{ph}}$  is derived as

$$\begin{aligned} \psi_{\text{ph}}(t) &= N_c \sum_{i=1}^{\kappa} (\varphi_i(t) + \varphi_l(t)) \\ &= N_c \sum_{i=1}^{\kappa} \left( \varphi_i(t) + \sum_{j=1}^{\gamma} \varphi_{lij}(t) + \sum_{j=1}^{\gamma} \varphi_{l(i+\tau)_j}(t) \right) \end{aligned} \quad (45)$$

where  $N_c$  and  $\kappa$  are, respectively, the number of turns of each coil and the coil number of each phase, respectively.  $\varphi_l$  represents the leakage flux in all slots and slot openings associated with the phase, which is obtained from the flux distribution in LPMCM.  $\gamma$  is the layer of the tangential magnetic reluctance in one slot.  $\varphi_{lij}$  and  $\varphi_{l(i+\tau)_j}$  are the tangential fluxes in the slot that can cover the phase coil [22]. It is also specified in Fig. 4.

The induced voltage is defined as the derivative of the flux linkage with respect to time under the on-load condition

$$U_{\text{ph}} = -\frac{d\psi_{\text{ph}}}{dt} \text{ ph} = A, B, C. \quad (46)$$

The electromagnetic torque is determined by Arkkio's method. It improves Maxwell's stress tensor method, whose

TABLE I  
MAIN PARAMETERS OF PROPOSED SPM MACHINES

Parameter	8-pole/48-slot	8-pole/9-slot	Unit
Stator outer radius	75	50	mm
Stator inner radius	45	26.5	mm
Airgap length	0.75	1	mm
Magnet thickness	4.5	3	mm
Rotor outer radius	44.25	25.5	mm
Shaft radius	17.5	17.5	mm
Stator yoke height	8	4.4	mm
Active length	75	50	mm
Slot opening	1.5	2	mm
Tooth body width	3.72	8.7	mm
Pole-arc to pole-pitch ratio	1	1	
Magnet remanence	1.26	1.2	T
Relative recoil permeability	1.07	1.05	
Magnetization	Parallel	Parallel	
Rated speed	1500	400	rpm
Number of pole pairs	4	4	
Number of slots	48	9	
Rated current (peak)	25	10	A
Lamination material	WG35WW300	Transil300	
Operation mode	BLAC	BLDC	

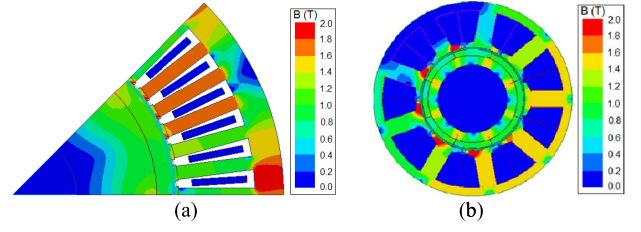


Fig. 10. Flux density distribution of SPM machines at rated current in the nonlinear FEM. (a) 8-pole/48-slot. (b) 8-pole/9-slot.



Fig. 11. 8-pole/9-slot prototype machine. (a) Stator. (b) Rotor.

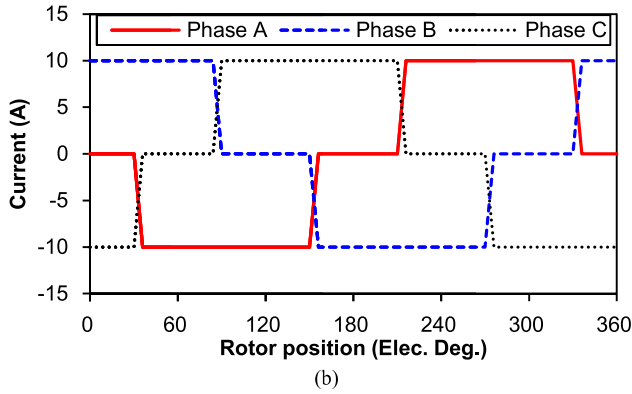
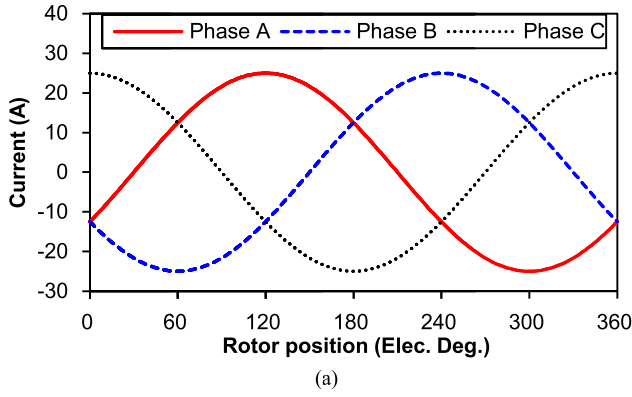


Fig. 9. Current waveforms of the SPM machines at rated load. (a) 8-pole/48-slot. (b) 8-pole/9-slot.

accuracy is affected by integration path in the air gap. Therefore, based on the predicted air-gap flux density, the total torque is computed by integrating over the surface in the air gap [24]

$$T = \frac{l_{ef}}{\mu_0(r_s - r_r)} \int_S r B_{sr}(\alpha, r, t) B_{sa}(\alpha, r, t) dS \quad (47)$$

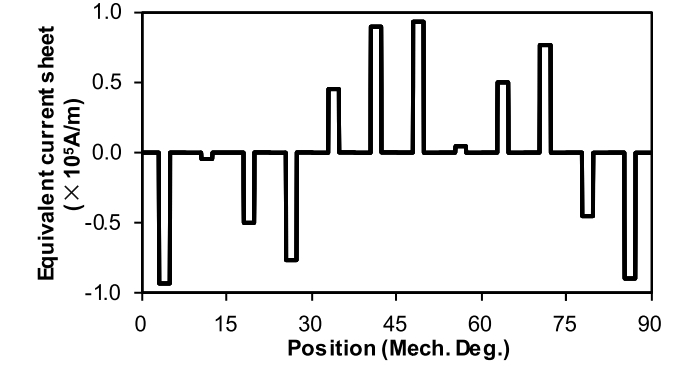


Fig. 12. Equivalent current sheet at stator bore of 8-pole/48-slot SPM machine.

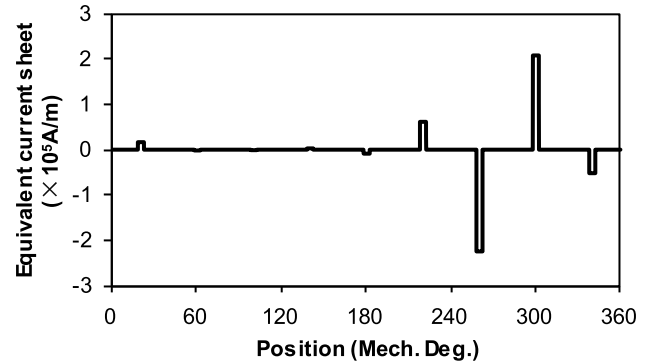


Fig. 13. Equivalent current sheet at stator bore of 8-pole/9-slot SPM machine.

where  $r$  and  $\alpha$  is the radius and angle of the integration surface element in the air gap.  $r_s$  and  $r_r$  are the outer and inner radius of the integration surface.

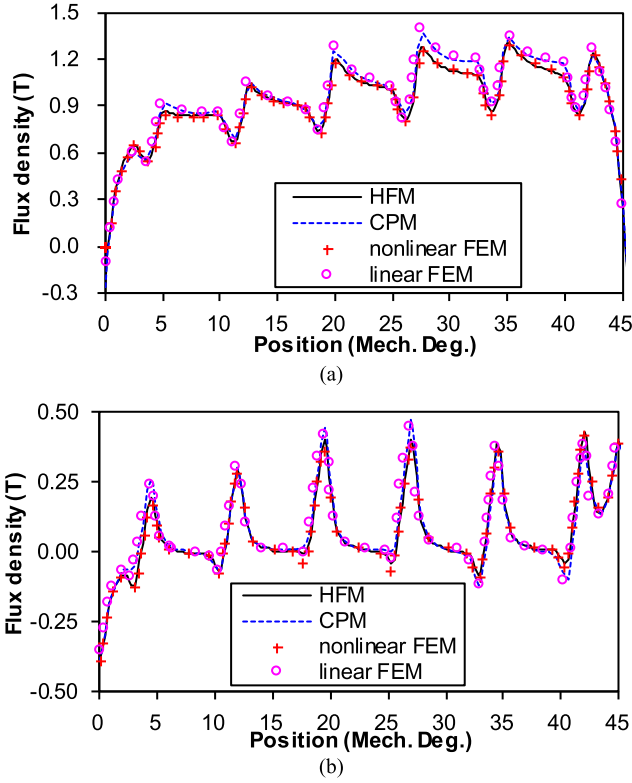


Fig. 14. Comparison of on-load flux densities computed by HFM, CPM, and FE methods at the middle air gap of 8-pole/48-slot SPM machine under rated load ( $I_{\text{peak}} = 25$  A). (a) Radial. (b) Circumferential.

#### IV. FE AND EXPERIMENTAL VALIDATION

In order to verify the proposed model, the FE analysis has been carried out on two, integer-slot (8-pole/48-slot) and fractional-slot (8-pole/9-slot), SPM machines, and the experiment has been done on the latter. It is noted that only 2-D FE analysis is performed, and therefore, the end effect is neglected. The  $B$ - $H$  curves of iron laminations in the nonlinear FEM for both machines are shown in Fig. 8, while the relative permeability of iron in the linear FEM is 1 000 000. The differences between nonlinear and linear FEM exhibit the nonlinearity effect. Table I shows the major parameters of these two machines. Fig. 9 illustrates that the 8-pole/48-slot machine is operated in the brushless alternating current mode while the other is in the brushless direct current mode. Fig. 10 shows the field distribution of both SPM machines in the nonlinear FEM, which also reveals the saturation level in the iron. Fig. 11 shows the stator and rotor of 8-pole/9-slot prototype, which is used for experimental validation.

Under the rated load, the armature reaction field increases the saturation level and HFM becomes more advantageous. Figs. 12 and 13 show the calculated equivalent current sheet for both machines. Then, the air-gap field distribution of both machines can be predicted by HFM and compared with CPM and FEM, Figs. 14 and 15. It can be seen that HFM can accurately predict the air-gap flux density while CPM always overestimates due to neglecting nonlinearity effect, especially for the radial air-gap flux density facing the

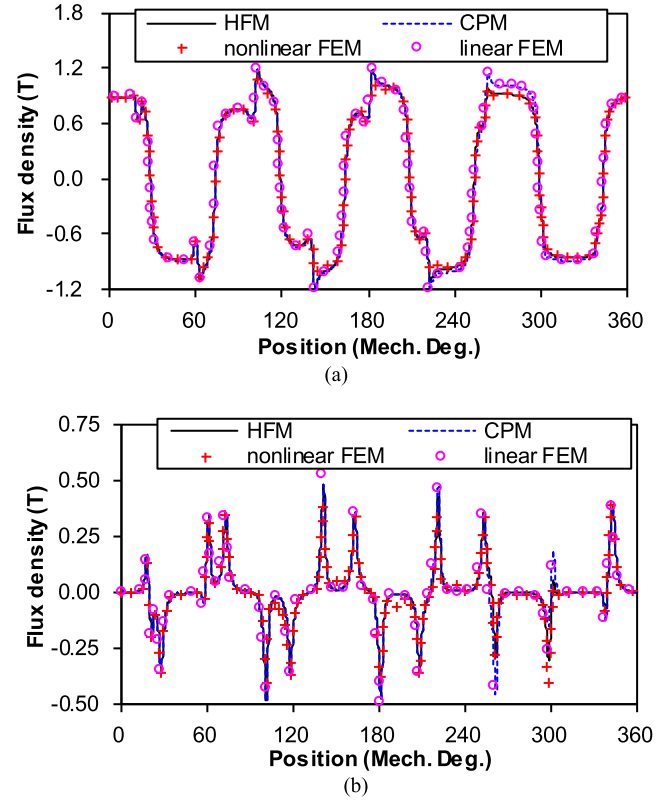


Fig. 15. Comparison of on-load air-gap flux densities computed by HFM, CPM, and FE methods at the middle air gap of 8-pole/9-slot SPM machine under rated load ( $I_{\text{peak}} = 10$  A). (a) Radial. (b) Circumferential.

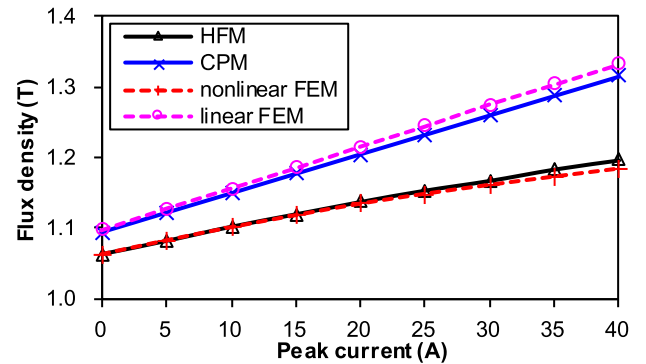


Fig. 16. Variation of average radial air gap flux density facing the fourth tooth with peak current of 8-pole/48-slot SPM machine.

fourth tooth of 8-pole/48-slot machine and facing the seventh tooth with 8-pole/9-slot machine. The linear FEM results are also higher than nonlinear FEM results, which show the influence of iron nonlinearity on the air gap field. Moreover, the average radial air-gap flux densities, facing the fourth tooth for the 48-slot machine and facing the seventh tooth for the 9-slot machine, are calculated by HFM, CPM, and FEM at different peak current, as shown in Figs. 16 and 17. The radial component of HFM predicted flux density agrees well with nonlinear FEM predictions at different peak current while the CPM-predicted flux densities are much higher than those predicted by nonlinear FEM but agree well with linear



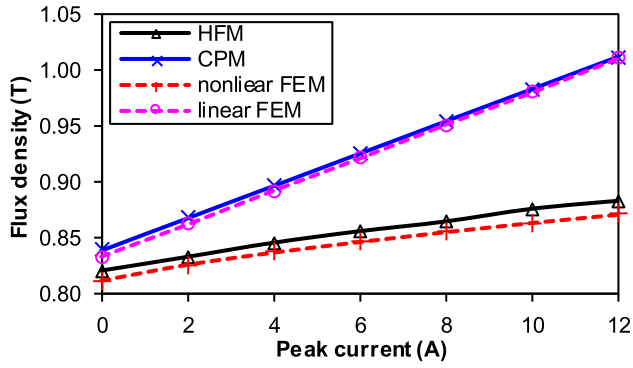


Fig. 17. Variation of average radial air gap flux density facing the seventh tooth with peak current of 8-pole/9-slot SPM machine.

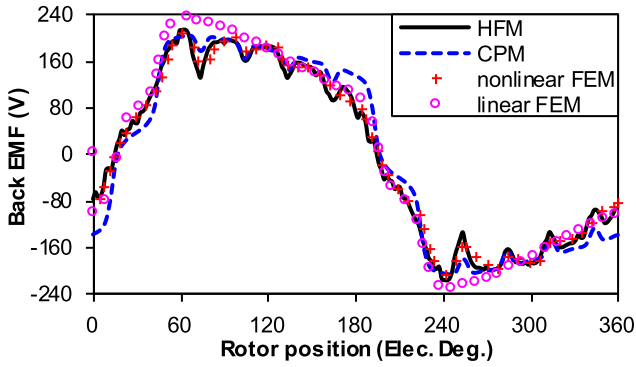


Fig. 18. HFM, CPM, and FE predicted induced voltage waveforms of 8-pole/48-slot SPM machine at rated current.

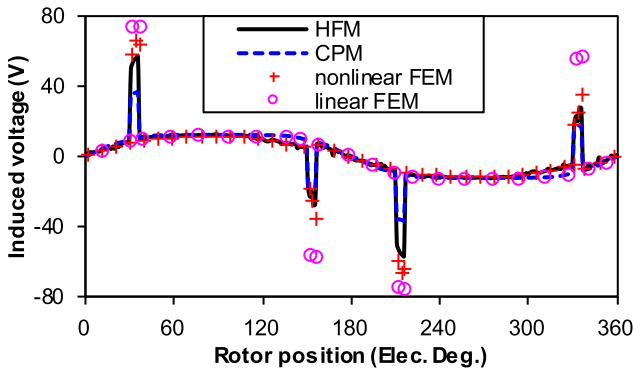
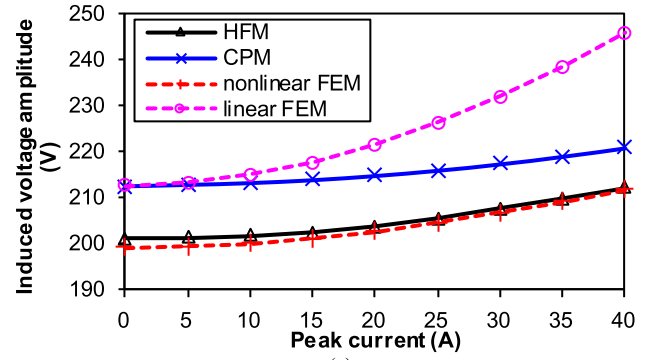


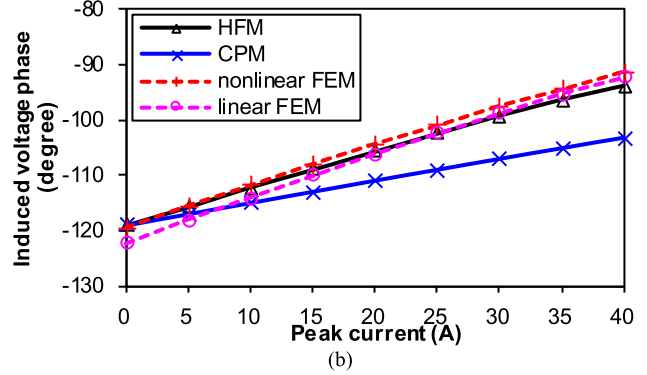
Fig. 19. HFM, CPM, and FE predicted induced voltage waveforms of 8-pole/9-slot SPM machine at rated current.

FEM results, as can be seen in both machines. Even under the open-circuit condition, the nonlinearity effect exists in both machines to influence the air-gap field [22].

As can be seen in Figs. 18 and 19, HFM has high accuracy for predicting the induced voltage waveform at the rated current while CPM exhibits large errors for both machines. The induced voltage of 8-pole/9-slot machine shown in Fig. 19 has a high surge voltage because the current waveform in the simulation is ideal and has unsmooth changes. Figs. 20 and 21 compare the amplitude and phase of the fundamental-induced voltage predicted by HFM, CPM,

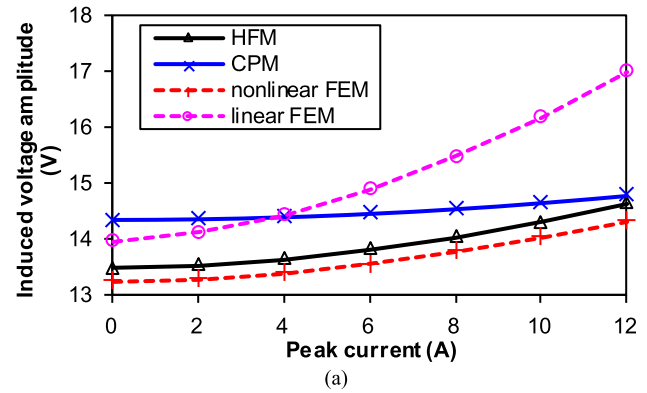


(a)

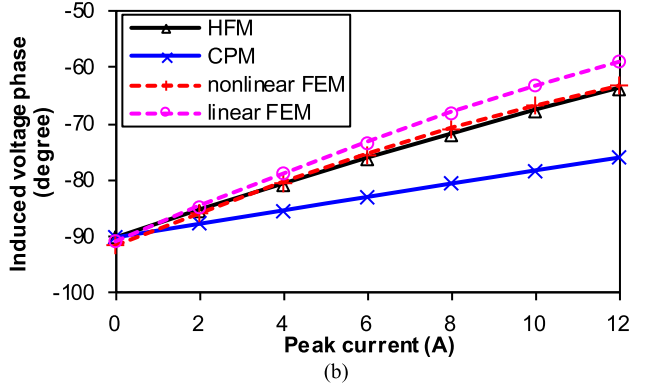


(b)

Fig. 20. Variation of amplitude and phase of the fundamental induced voltage with peak current of 8-pole/48-slot SPM machine. (a) Amplitude. (b) Phase.



(a)



(b)

Fig. 21. Variation of amplitude and phase of the fundamental induced voltage with peak current of 8-pole/9-slot SPM machine. (a) Amplitude. (b) Phase.

and FE method at different peak current. Again, HFM shows much higher accuracy than CPM. Such advantage of HFM is attributed to its inclusion of flux leakage and nonlinearity

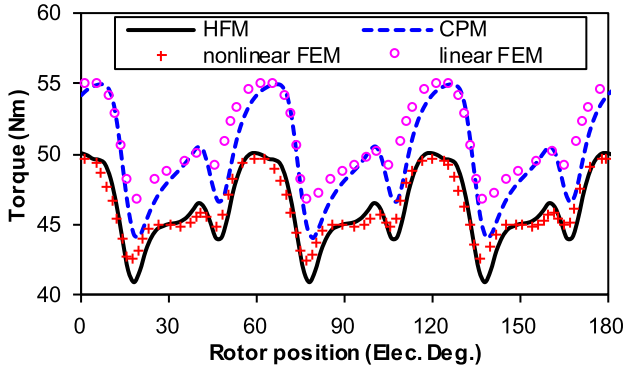


Fig. 22. Torque waveforms of 8-pole/48-slot SPM machine at rated current.

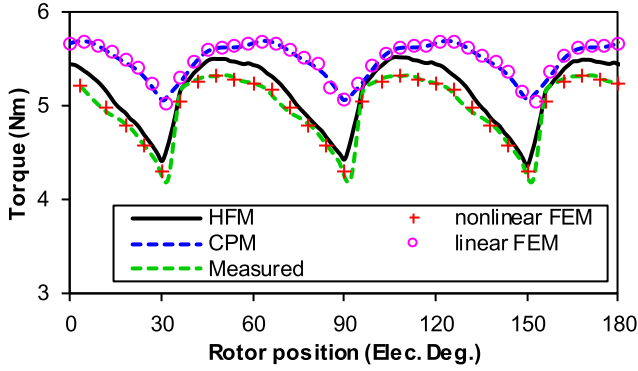


Fig. 23. Torque waveform of 8-pole/9-slot machine at rated current.

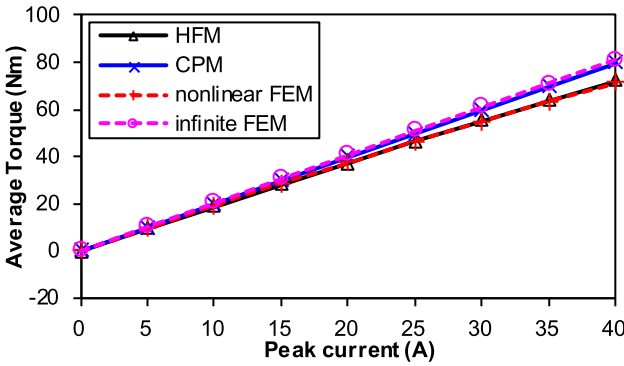


Fig. 24. Variation of average torque with peak current of 8-pole/48-slot SPM machine.

effect. In addition, when comparing the nonlinear and linear FEM results from Figs. 18–21, it can be seen that the iron nonlinearity has a significant influence on the induced voltage.

As shown in Figs. 22 and 23, the torque waveform predicted by HFM agrees well with FE prediction at rated current while CPM overestimates it for both machines. The measured torque of 8-pole/9-slot machine also confirms the high accuracy of HFM in Fig. 23. Moreover, as shown in Figs. 24 and 25, the average torque predicted by HFM achieves excellent accuracy at different load current while the error of CPM prediction gradually becomes larger with the increase of load. It can also be seen from the nonlinear and linear FEM results in

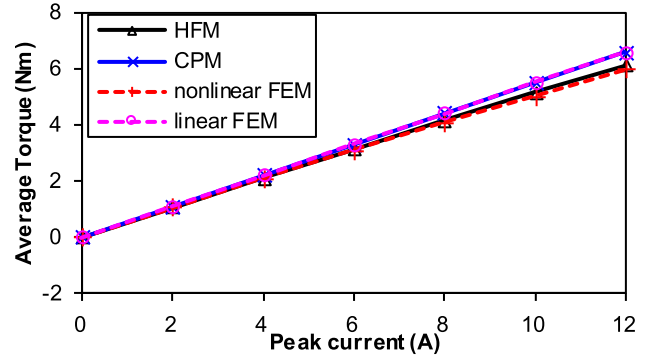


Fig. 25. Variation of average torque with peak current of 8-pole/9-slot SPM machine.

TABLE II  
CALCULATION TIME OF 8-POLE/48-SLOT SPM MACHINE

Current (A) Time (s) Model	0	5	10	15	20	25	30	35	40
CPM	1.1	1.0	1.0	1.1	1.0	1.0	1.0	1.0	1.0
HFM	50.3	42.4	41.5	38.5	38.0	44.3	48.2	44.3	43.8
FEM, nonlinear	537	534	579	577	537	535	543	550	541

TABLE III  
CALCULATION TIME OF 8-POLE/9-SLOT SPM MACHINE

Current (A) Time (s) Model	0	2	4	6	8	10	12
CPM	1.8	1.8	1.7	1.6	1.6	1.7	1.7
HFM	44.9	44.9	43.3	42.2	43.7	44.2	45.0
FEM, nonlinear	650	671	637	679	672	652	657

TABLE IV  
MAIN PARAMETER SETTING OF SIMULATION

Machine model	Airgap segment	Simulation steps	node
8-pole/ 48-slot	CPM	720	0
	HFM		120
	FEM		17965
8-pole/ 9-slot	CPM	480	0
	HFM		90
	FEM		33035

Figs. 22–25 that the iron nonlinearity will decrease the torque of SPM machines

In order to compare the computational speeds of HFM, CPM, and nonlinear FEM, their calculation times in one electric period for all the machines are compared and analyzed in Tables II and III. It is noted that FEM results of both machines are solved in Ansys Maxwell, while CPM and HFM calculations are performed in MATLAB. The main parameter setting of simulation is shown in Table IV. It can be seen that CPM is the fastest while FEM is the slowest for both machines. HFM calculation runs at least 10× faster than FEM simulation for both machines. This advantage will significantly improve the efficiency of machine design.

## V. CONCLUSION

A HFM integrating CPM and LPMCM has been developed for analyzing SPM machines considering nonlinearity effect and tooth tips. The nonlinearity of the stator yoke and tooth body is represented by the equivalent current on the slot opening while the tooth-tip saturation is accounted for by additional equivalent current sheet on the tooth surface. Based on such equivalent currents, the permeability of the iron can be regarded as infinite and superposition theory can be applied to calculate the on-load air-gap field produced by PMs, winding, and equivalent currents. In order to calculate the equivalent current, a solving procedure is introduced to guarantee the convergence. Then, the air-gap field distribution, induced voltage, and torque are all obtained from HFM. HFM has higher accuracy than CPM in predicting the air-gap field and electromagnetic performance when the iron material in the machine works around the nonlinear region. It is demonstrated by both the FE analysis and experiment. Based on HFM, other machines such as inset PM machines and IPM machines will be investigated in the future.

## ACKNOWLEDGMENT

This work was supported in part by the National Natural Science Foundation of China under Grant 51677169 and Grant 51637009 and in part by the Fundamental Research Funds for the Central Universities under Grant 2017QNA4016.

## REFERENCES

- [1] Z. Q. Zhu and D. Howe, "Electrical machines and drives for electric, hybrid, and fuel cell vehicles," *Proc. IEEE*, vol. 95, no. 4, pp. 746–765, Apr. 2007.
- [2] S. Ruoho, T. Santa-Nokki, J. Kolehmainen, and A. Arkkio, "Modeling magnet length in 2-D finite-element analysis of electric machines," *IEEE Trans. Magn.*, vol. 45, no. 8, pp. 3114–3120, Aug. 2009.
- [3] Z. Q. Zhu, D. Howe, E. Bolte, and B. Ackermann, "Instantaneous magnetic field distribution in brushless permanent magnet DC motors, part I: Open-circuit field," *IEEE Trans. Magn.*, vol. 29, no. 1, pp. 124–135, Jan. 1993.
- [4] Z. Q. Zhu and D. Howe, "Instantaneous magnetic field distribution in brushless permanent magnet DC motors, part II: Armature-reaction field," *IEEE Trans. Magn.*, vol. 29, no. 1, pp. 136–142, Jan. 1993.
- [5] D. Žarko, D. Ban, and T. A. Lipo, "Analytical calculation of magnetic field distribution in the slotted air gap of a surface permanent-magnet motor using complex relative air-gap permeance," *IEEE Trans. Magn.*, vol. 42, no. 7, pp. 1828–1837, Jul. 2006.
- [6] T. C. O'Connell and P. T. Krein, "A Schwarz–Christoffel-based analytical method for electric machine field analysis," *IEEE Trans. Energy Convers.*, vol. 24, no. 3, pp. 565–577, Sep. 2009.
- [7] K. Boughrara, R. Ibtiouen, D. Žarko, O. Touhami, and A. Rezzoug, "Magnetic field analysis of external rotor permanent-magnet synchronous motors using conformal mapping," *IEEE Trans. Magn.*, vol. 46, no. 9, pp. 3684–3693, Sep. 2010.
- [8] K. Ramakrishnan, D. Žarko, A. Hanic, and G. Mastinu, "Improved method for field analysis of surface permanent magnet machines using Schwarz–Christoffel transformation," *IET Electr. Power Appl.*, vol. 11, no. 6, pp. 1067–1075, Jul. 2017.
- [9] L. J. Wu, Z. Q. Zhu, D. Staton, M. Popescu, and D. Hawkins, "An improved subdomain model for predicting magnetic field of surface-mounted permanent magnet machines accounting for tooth-tips," *IEEE Trans. Magn.*, vol. 47, no. 6, pp. 1693–1704, Jun. 2011.
- [10] T. A. Driscoll, "Schwarz–Christoffel toolbox user's guide: Version 2.3," Univ. Delaware, Newark, DE, USA, 2005.
- [11] V. Ostović, *Dynamics of Saturated Electric Machines*. New York, NY, USA: Springer-Verlag, 1989.
- [12] X. Huang, M. Zhu, W. Chen, J. Zhang, and Y. Fang, "Dynamic reluctance mesh modeling and losses evaluation of permanent magnet traction motor," *IEEE Trans. Magn.*, vol. 53, no. 6, Jun. 2017, Art. no. 8102804.
- [13] A. Dalal and P. Kumar, "Analytical model for permanent magnet motor with slotting effect, armature reaction, and ferromagnetic material property," *IEEE Trans. Magn.*, vol. 51, no. 12, Dec. 2015, Art. no. 8114910.
- [14] F. R. Alam and K. Abbaszadeh, "Magnetic field analysis in eccentric surface-mounted permanent-magnet motors using an improved conformal mapping method," *IEEE Trans. Energy Convers.*, vol. 31, no. 1, pp. 333–344, Mar. 2016.
- [15] K. Abbaszadeh and F. Rezaee-Alam, "On-load field component separation in surface-mounted permanent-magnet motors using an improved conformal mapping method," *IEEE Trans. Magn.*, vol. 52, no. 2, Feb. 2016, Art. no. 5200112.
- [16] F. Rezaee-Alam, B. Rezaeealam, and J. Faiz, "Unbalanced magnetic force analysis in eccentric surface permanent-magnet motors using an improved conformal mapping method," *IEEE Trans. Energy Convers.*, vol. 32, no. 1, pp. 146–154, Mar. 2017.
- [17] L. Zhu, S. Z. Jiang, Z. Q. Zhu, and C. C. Chan, "Analytical modeling of open-circuit air-gap field distributions in multisegment and multilayer interior permanent-magnet machines," *IEEE Trans. Magn.*, vol. 45, no. 8, pp. 3121–3130, Aug. 2009.
- [18] J. R. Anglada and S. M. Sharkh, "Analytical calculation of the torque produced by transverse flux machines," *IET Electr. Power Appl.*, vol. 11, no. 7, pp. 1298–1305, Aug. 2017.
- [19] P. Jalali, S. T. Boroujeni, and N. Bianchi, "Analytical modeling of slotless eccentric surface-mounted PM machines using a conformal transformation," *IEEE Trans. Energy Convers.*, vol. 32, no. 2, pp. 658–666, Jun. 2017.
- [20] A. Hanic, D. Žarko, and Z. Hanic, "A novel method for no-load magnetic field analysis of saturated surface permanent-magnet machines using conformal mapping and magnetic equivalent circuits," *IEEE Trans. Energy Convers.*, vol. 31, no. 2, pp. 740–749, Jun. 2016.
- [21] A. Hanic, D. Žarko, D. Kuhinek, and Z. Hanic, "On-load analysis of saturated surface permanent magnet machines using conformal mapping and magnetic equivalent circuits," *IEEE Trans. Energy Convers.*, vol. 33, no. 3, pp. 915–924, Sep. 2018.
- [22] L. J. Wu, Z. Li, X. Huang, Y. Zhong, Y. Fang, and Z. Q. Zhu, "A hybrid field model for open-circuit field prediction in surface-mounted PM machines considering saturation," *IEEE Trans. Magn.*, vol. 54, no. 6, Jun. 2018, Art. no. 8103812.
- [23] Z. Q. Zhu, D. Howe, and C. C. Chan, "Improved analytical model for predicting the magnetic field distribution in brushless permanent-magnet machines," *IEEE Trans. Magn.*, vol. 38, no. 1, pp. 229–238, Jan. 2002.
- [24] A. Arkkio, "Analysis of induction motors based on the numerical solution of the magnetic field and circuit equations," *Acta Polytech. Scand. Electr. Eng. Ser.*, no. 59, pp. 3–97, 1987.
- [25] L. J. Wu, Z. Q. Zhu, D. A. Staton, M. Popescu, and D. Hawkins, "Comparison of analytical models of cogging torque in surface-mounted PM machines," *IEEE Trans. Ind. Electron.*, vol. 59, no. 6, pp. 2414–2425, Jun. 2012.
- [26] Z. Azar, Z. Q. Zhu, and G. Ombach, "Influence of electric loading and magnetic saturation on cogging torque, back-EMF and torque ripple of PM machines," *IEEE Trans. Magn.*, vol. 48, no. 10, pp. 2650–2658, Oct. 2012.
- [27] Z. Q. Zhu and D. Howe, "Instantaneous magnetic field distribution in permanent magnet brushless DC motors, part IV: Magnetic field on load," *IEEE Trans. Magn.*, vol. 29, no. 1, pp. 152–158, Jan. 1993.
- [28] P. Jalali, S. T. Boroujeni, and N. Bianchi, "Simple and efficient model for slotless eccentric surface-mounted PM machines," *IET Electr. Power Appl.*, vol. 11, no. 4, pp. 631–639, Apr. 2017.